Journal of Materials Chemistry B

ROYAL SOCIETY OF CHEMISTRY

PAPER

View Article Online
View Journal | View Issue

Cite this: J. Mater. Chem. B, 2025, 13, 5163

Dual-color reversible fluorescent carbon dots designed for dynamic monitoring of cellular superoxide anion radicals†

Dan Wang,*[a] Yanke Zhai,[b] Yun Wang,[c] Xu Fu,*[c] Yibing Ji *[ab] and Ruijun Li *[ab]

Received 15th January 2025,
Accepted 3rd April 2025

DOI: 10.1039/d5tb00099h

rsc.li/materials-b

The superoxide anion radical ($O_2^{\bullet-}$) represents the primary reactive oxygen species generated in biological systems. Real-time monitoring of its dynamic fluctuations provides valuable insights into disease progression and enables early diagnosis of hepatic ischemia-reperfusion injury (HIRI). In this work, we developed a novel dual-color fluorescent carbon dot (CD) probe through a one-step hydrothermal synthesis for reversible $O_2^{\bullet-}$ detection. The CDs demonstrated excellent sensitivity, dynamically detecting $O_2^{\bullet-}$ concentrations ranging from 0 to 60 μM with a detection limit of 0.56 μM. The probe exhibited remarkable reversibility, maintaining stable performance through at least three complete oxidation–reduction cycles following glutathione (GSH) treatment. In practical applications, the CDs achieved 95.2–104% recovery rates when detecting $O_2^{\bullet-}$ in serum samples. Cellular imaging experiments confirmed the probe's effectiveness in normal hepatocytes (LO2), showing clear reversible responses to $O_2^{\bullet-}$ fluctuations. Application in a HIRI cell model revealed significant elevation of $O_2^{\bullet-}$ levels and provided new evidence for its role in HIRI-related signaling pathways. This study not only presents an effective dual-color fluorescent probe for dynamic $O_2^{\bullet-}$ monitoring but also establishes a versatile synthetic strategy that could be adapted for imaging other biologically relevant molecules in living cells.

Introduction

Hepatic ischemia-reperfusion injury (HIRI) is characterized by a transient interruption of hepatic blood flow resulting in tissue hypoxia, followed by subsequent reperfusion that paradoxically exacerbates liver damage,[1,2] which occurs mainly during partial hepatectomy, trauma, resuscitation from haemorrhagic shock, liver transplantation, and other clinical procedures.[3,4] Since hepatic energy production is dependent on the supply of oxygen and mitochondrial function, hepatic function is obviously suppressed and impaired in ischemia and hypoxia,[5,6] and the subsequent reoxygenation of the tissues by reperfusion of the blood flow triggers an even more severe oxidative stress and inflammation, leading to liver injury.[7,8] Therefore, in-depth understanding of the pathogenic mechanism of oxidative stress regulation is beneficial to the early diagnosis and treatment of HIRI.[9]

Oxidative stress and redox imbalance are closely linked to the advancement of HIRI.[10] Oxidative stress results from an imbalance in the cellular redox state caused by the accumulation of reactive oxygen species (ROS), The accumulation of ROS disrupts the cellular redox balance, leading to oxidative stress,[11] lipid peroxidation, DNA damage, oxidative inactivation of proteins, and eventually cell death.[12] $O_2^{\bullet-}$, the body's first ROS produced, is an important marker of HIRI that can participate in downstream protein oxidation leading to apoptosis or necrosis.[13,14] Therefore, monitoring the changes of $O_2^{\bullet-}$ levels in cells can accurately assess the extent of HIRI and provide insight into the molecular mechanisms of HIRI.

Fluorescence imaging technology is widely employed in cell biology due to its high sensitivity, low detection limit, ability to detect signaling molecules at physiological concentrations, and excellent temporal-spatial resolution.[15–17] Fluorescent probes serve as powerful tools for imaging target substances and monitoring their microenvironmental changes.[18] Currently, hundreds of fluorescent probes have been developed for ROS detection, typically relying on oxidative cleavage of chemical bonds at active sites. However, these probes undergo irreversible structural changes upon reacting with ROS, preventing long-term tracking of dynamic ROS fluctuations during pathological processes.[19–22] In contrast, reversible fluorescent

[a] Department of Analytical Chemistry, China Pharmaceutical University, Nanjing 210009, China
[b] Key Laboratory of Drug Quality Control and Pharmacovigilance, Ministry of Education, Nanjing 210009, China. E-mail: ccjlrj@cpu.edu.cn, jiyibing@msn.com
[c] Laboratory of Emergency Medicine, Lanzhou University Second Hospital, Gansu, Lanzhou, 730000, China. E-mail: fuxu0910@163.com

† Electronic supplementary information (ESI) available. See DOI: https://doi.org/10.1039/d5tb00099h

probes offer distinct advantages, including reusability, high selectivity, real-time dynamic monitoring capability, and resistance to interference.[23,24] Thus, developing real-time, dynamic, and reversible fluorescent probes for ROS quantification is essential. Although a few small-molecule fluorescent probes have been designed for reversible $O_2^{\bullet-}$ monitoring.[25–27] Their synthesis and purification processes are often complex and labor-intensive.[28] In contrast, carbon dots (CDs) usually have good photoluminescent properties, biocompatibility, photochemical stability, and ease of preparation.[29–31] A CDs for the reversible detection of $O_2^{\bullet-}$ in cells as well was reported. Zhang *et al.* has designed and synthetized fluorescent Te-CDs to dynamically and reversibly image the change of $O_2^{\bullet-}$ concentration in depressed mice, in which Te was the active site.[32] Nevertheless, such probes emit only green or yellow fluorescence and are monochromatic, suffering from strong autofluorescence interference, high background noise, and potential photodamage—factors that limit their biomedical applications. Therefore, developing effective $O_2^{\bullet-}$-responsive CDs with both long-wavelength emission and dual-color fluorescence properties would significantly enhance bioimaging applications. Such probes offer multiple advantages, including deeper tissue penetration, minimal phototoxicity, and reduced interference with biological molecules.

In this study, we developed dual-color fluorescent CDs for dynamic and reversible detection of $O_2^{\bullet-}$ through rational design. The CDs were synthesized *via* a one-step hydrothermal method using 4,4′,4″,4‴-(porphine-5,10,15,20-tetrayl) tetrakis(benzoic acid) (TCPP) and caffeic acid (CA) as precursors. The resulting CDs possess surface catechol residues that enable reversible quinone/phenol transitions, forming the basis for a redox-reversible sensor with outstanding selectivity and sensitivity toward $O_2^{\bullet-}$. These CDs demonstrated excellent performance in both *in vitro* and cellular applications, showing reversible $O_2^{\bullet-}$ detection within the 0–60 μM concentration range and enabling real-time monitoring of dynamic $O_2^{\bullet-}$ fluctuations in living cells. Using this probe, we successfully observed significantly elevated $O_2^{\bullet-}$ levels in hepatic ischemia-reperfusion injury (HIRI) cells, suggesting $O_2^{\bullet-}$ may serve as a potential biomarker for HIRI. Our investigation further explored the relevant signaling pathways and clarified $O_2^{\bullet-}$ regulatory role in HIRI progression. Beyond serving as an effective visualization tool for HIRI studies, these CDs with their superior properties may open new possibilities for nanomaterial-based clinical diagnosis of various liver disorders.

Experimental section

Synthesis of the dual-color fluorescent CDs

Solvothermal preparation was used to create CDs. 10 mL of DMF was mixed with 50 mg of CA and 15 mg of TCPP. A magnetic stirrer was used to agitate the liquid, and ultrasonography was used to create a homogenous solution. The mixture was then moved to a Teflon-line autoclave and cooked for 12 hours at 160 °C, turning it into a reddish-brown liquid. The solution was dialyzed (MWCO: 1000 Da) against deionized water for 12 hours after being filtered through a 0.22 μm filter membrane. After being freeze-dried, the powder was distributed in deionized water and kept at 4 °C.

Concentration detection of $O_2^{\bullet-}$ by dual-color fluorescent CDs

Different concentrations of $O_2^{\bullet-}$ solution were added to PBS buffer (50 mM, pH = 7.4) containing CDs (diluted 10-fold, 100 μL) in order to examine the impact of these concentrations on the fluorescence of CDs. For ten minutes, the mixture was incubated at 37 °C. At last, the excitation at 390 nm was used to record the fluorescence spectra.

$O_2^{\bullet-}$ concentration measurement in human serum

The human serum samples had normal liver function and were taken from Lanzhou University's Second Affiliated Hospital. Prior to testing, the serum samples were 20 times diluted with deionized water. A series of serum spiked samples were then prepared by adding varying concentrations of $O_2^{\bullet-}$ solution. The remainder of the reaction process and detection technique was the same as that of $O_2^{\bullet-}$.

Establishment of HIRI cell model

The sugar-free anaerobic preconditioning-reperfusion experiment was used to create the HIRI cell model. After the culture medium was removed and the cells were cultured in high-sugar DMEM containing 10% fetal bovine serum for 30 minutes, the protocol was as follows: LO2 cells were first cultured in sugar-free serum-free DMEM medium treated with the deoxidizing agent sodium dithionite (0.5 mM) for 30 minutes.[33]

Results and discussion

Designing of CDs

Catechol has been widely employed as a reactive site in organic probes for the dynamic and reversible detection of $O_2^{\bullet-}$. The underlying detection mechanism involves the oxidation of catechol to *o*-benzoquinone.[34] Inspired by this principle, we utilized catechol and as precursors for the synthesis of CDs. TCPP, a porphyrin derivative, serves as both a fluorescence emission center and a structural framework due to its intrinsic conjugated system. Additionally, it facilitates the carbonization process during CDs synthesis *via* dehydration and carbonylation.[35] Meanwhile, CA was incorporated as a recognition moiety to enable $O_2^{\bullet-}$ responsiveness. The hydrothermal polycondensation and carbonization of CA and TCPP yielded long-wavelength-emitting CDs, as the reaction promoted the formation of extended conjugated aromatic structures. Subsequent high-pressure and high-temperature conditions induced partial cleavage, exposing residual catechol groups on the CDs surface, thereby preserving their $O_2^{\bullet-}$ sensitivity. This strategy ultimately enabled the successful synthesis of long-wavelength fluorescent CDs with reversible $O_2^{\bullet-}$ responsiveness. (Scheme 1).

Characterizations of CDs

In order to understand their morphology and composition, the synthesized dual-color fluorescent CDs were characterized

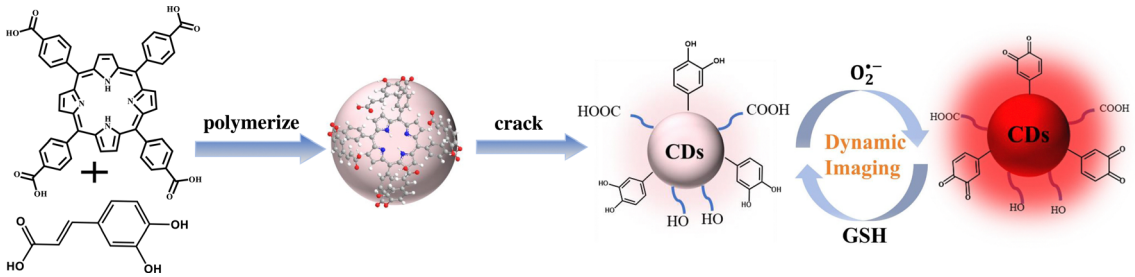

Scheme 1 Diagram showing the production route and detecting technique for CDs.

using transmission electron microscopy (TEM), Fourier transform infrared spectroscopy (FT-IR) and X-ray photoelectron spectroscopy (XPS). Key information on the functional groups and organic properties of CDs was provided by these characterization tools and confirmed the successful synthesis of dual-color fluorescent CDs.

The TEM images (Fig. 1a and b) revealed that the CDs possessed a spherical morphology with uniform size distribution, showing no obvious aggregation. The CDs exhibited a spherical shape with an average diameter of approximately 2.5 nm. In addition, the high-resolution transmission electron microscopy (HRTEM) images of CDs clearly showed lattice streaks with a crystallographic spacing of 0.11 nm (Fig. 1a), this spacing was inconsistent with the lattice spacing of graphene corresponding to the (100) face (0.21) and corresponding to the (002) face (0.32 nm). It is speculated that the reason for this may be that the carbon nuclei of CDs was formed by processes such as condensation and carbonization, which have a great influence on the lattice spacing of CDs. These results confirmed the successful synthesis of CDs by solvothermal method.

As shown in Fig. 1c, The O–H and N–H stretching vibration peaks near 3313 cm^{-1}, the C=O stretching vibration peak associated with –COOH at 1690 cm^{-1}, and the aromatic structural contraction vibration peaks of the porphyrin ring at 1606 cm^{-1} and 1400 cm^{-1} were all seen in the FT-IR of TCPP. The O–H stretching vibration peak near 3430 cm^{-1}, the C=O stretching vibration peak associated with –COOH at 1650 cm^{-1},

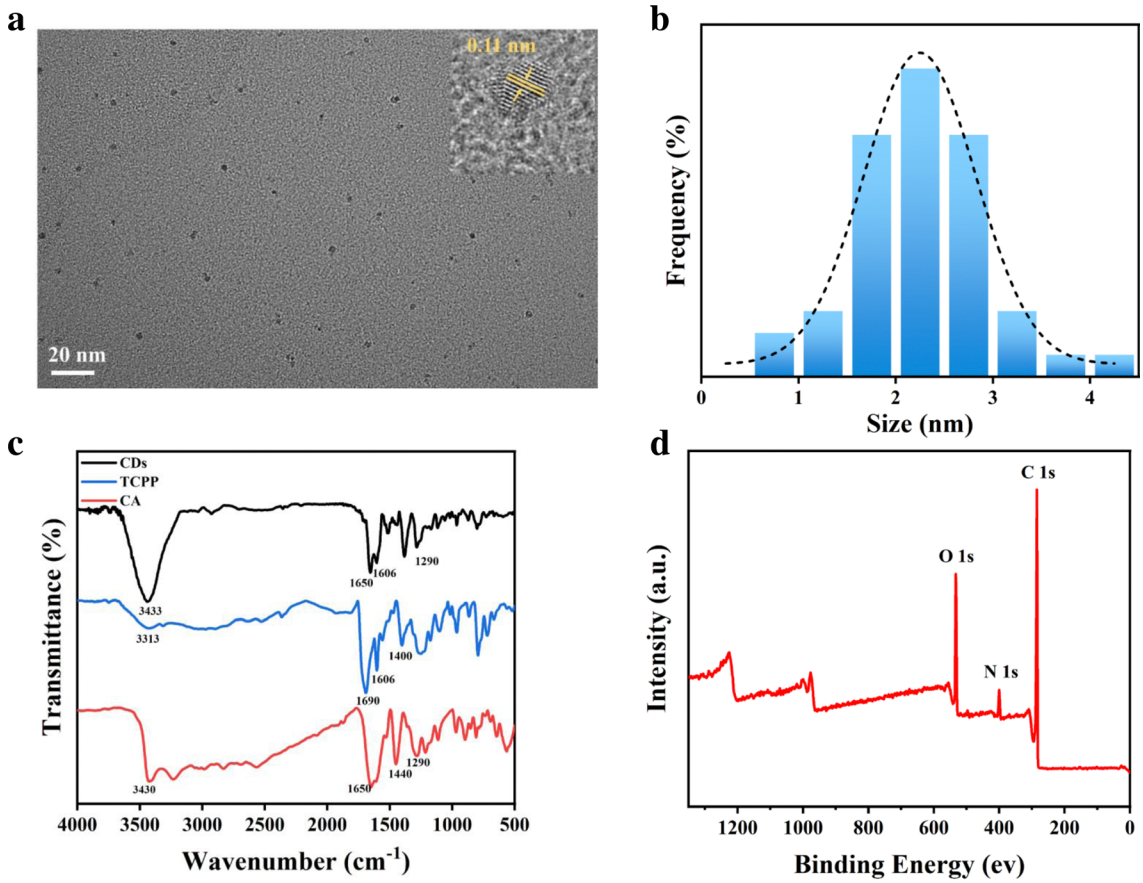

Fig. 1 (a) CDs with TEM and HRTEM images. (b) The size of CD particles. (c) FT-IR of CDs. (d) XPS spectrum of CDs.

the C=C stretching vibration at 1440 cm^{-1}, and the C–O stretching vibration at 1290 cm^{-1} were all seen in the FT-IR of *ca.* In the FT-IR of CDs, the characteristic peak of C–O bond at 1290 cm^{-1}, the O–H stretching vibration near 3433 cm^{-1}, the C=O stretching vibration belonging to –COOH (1650 cm^{-1}) was also observed, as well as the contraction vibration of the aromatic structure attributed to the porphyrin ring (1606 cm^{-1}). All above results confirmed that both SA and TCPP were involved in the synthesis of CDs as precursors, and the CDs possessed functional groups such as –OH, C=C, and –COOH on their surfaces, and the porphyrin ring structure was present in the CDs.

XPS analysis was performed to further investigate the elemental composition of the CDs. The full-range XPS spectrum (Fig. 1d) revealed distinct peaks corresponding to C 1s, N 1s, and O 1s, confirming the presence of carbon, nitrogen, and oxygen in the CDs. High-resolution XPS spectra were subsequently analyzed for each element. Suggesting the existence of C, N, and O elements in the CDs. After that, the high-resolution XPS spectra of the various elements were examined. As shown in Fig. S1a (ESI†), the three peaks in the high-resolution C 1s spectra correspond to the C=O (287.97 eV), C–C (284.79 eV), and C–O/C–N (286.12 eV) bonds, respectively. Conversely, the C=O and C–O bonds were represented by the O 1s spectra. (Fig. S1b, ESI†). The N 1s spectra showed two peaks representing C–N and N–H bonds (Fig. S1c, ESI†), respectively, which suggested that CDs contain carboxylic acid portions and hydroxyl groups, the successful participation of CA and TCPP in the synthesis of CDs. The XPS full energy spectrum of CDs clearly demonstrates the chemical bonding composition and its bonding sites. The presence of these functional groups and chemical bonds is necessary to understand the properties and potential applications of CDs in biosensing and imaging. These results confirmed the presence of particular surface groups on CDs and were consistent with the FT-IR results.

Spectral behaviors of CDs

A thorough investigation of the spectral characteristics of CDs produced the results displayed in Fig. S2a (ESI†), The strong peaks in the UV-vis spectra near 295 nm were ascribed to the π–π* transitions of C=C and C=N, while the weak bands centered at 415 nm indicated the extended conjugated structure resulting from aromatic rings.[36,37] The fluorescence behavior of CDs under various excitation wavelengths was shown in Fig. S2b (ESI†). Maximum emission from CDs was observed at 485 nm and 650 nm under 390 nm excitation. The synthesized CDs exhibited excitation-independent behavior when the excitation wavelength was varied from 350 nm to 420 nm. This excitation-independent fluorescence was typically attributed to the relatively uniform surface state and narrow size distribution of the CDs.

CDs analytical performance for $O_2^{\bullet-}$ and reversibility of CDs

First, the reaction time was optimized at pH 7.4. As shown in Fig. S3 (ESI†), the I_{650}/I_{485} ratio reached its maximum at 10 min, with no significant change observed upon further extension of the reaction time. Therefore, the optimal incubation time for the reaction system was determined to be 10 min. Subsequently, under these optimized conditions, the sensor's analytical performance—including linearity, limit of detection (LOD), and selectivity—was evaluated. The fluorescence intensity of the CDs at 650 nm (under 390 nm excitation) gradually increased with higher $O_2^{\bullet-}$ concentrations, while the intensity at 485 nm remained constant (Fig. 2a). A linear relationship between $O_2^{\bullet-}$ activity and the I_{650}/I_{485} ratio was established: I_{650}/I_{485} = 0.064c + 4.71 (R^2 = 0.997),with an LOD of 0.56 μM and a linear range of 0–60 μM (Fig. 2b). This sensor's LOD for $O_2^{\bullet-}$ detection is superior to most reported methods. The fluorescence lifetimes of the CDs were measured both with and without $O_2^{\bullet-}$. While the lifetime at 485 nm showed only a minor change (Δ = 0.12 ns), the lifetime at 650 nm increased from 9.17 ns to 10.2 ns upon $O_2^{\bullet-}$ addition (Fig. S4, ESI†). These results are consistent with the proposed CDs/$O_2^{\bullet-}$ sensing mechanism.

To evaluate CDs' capacity to reversibly and dynamically detect $O_2^{\bullet-}$ (Fig. 2c). The addition of GSH and $O_2^{\bullet-}$ to CDs was done in turn, and after adding 50 μM $O_2^{\bullet-}$, the fluorescence ratio of the CDs increased. When 0.5 mM GSH was added to the aforementioned solution ten minutes later,[38] the fluorescence ratio returned to its starting point. The same procedure was repeated three times with the same results, demonstrating that CDs was capable of dynamically and reversibly detecting changes in $O_2^{\bullet-}$ concentration. Overall, the prepared CDs are

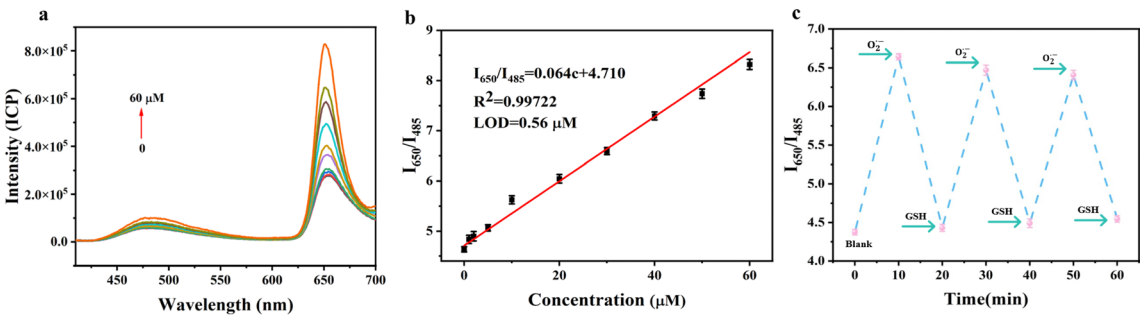

Fig. 2 (a) CDs/$O_2^{\bullet-}$ sensing system's fluorescence spectra in response to $O_2^{\bullet-}$ concentrations (0–60 μM). (b) The corresponding fitting curves for I_{650}/I_{485} and $O_2^{\bullet-}$ concentrations (0–60 μM). (c) Reversibility of CDs fluorescence in the presence of alternating treatments with 50 μM $O_2^{\bullet-}$ and 0.5 mM GSH.

sufficiently feasible for reversible detection of $O_2^{\bullet-}$ in aqueous solutions and have a high potential to be applied to complex living systems.

Selectivity and light stability of CDs

To investigate the selectivity of CDs for $O_2^{\bullet-}$, other competitive ROS, metal ions, amino acids and other active species were subjected to fluorescence response assays. CDs was reacted with various metal ions, amino acids, and ROS at pH 7.4 and incubation time of 10 min, respectively. The specific concentrations of the various active species in Section S2 of the ESI.† The fluorescence of CDs was unaffected by mixing with the above active species and showed weak fluorescence. The fluorescence intensity was significantly enhanced when and only when CDs reacted with $O_2^{\bullet-}$ (Fig. 3a). Coexisting ion experiments also showed that the fluorescence of CD reacting with $O_2^{\bullet-}$ was unaffected by ROS, various metal ions, and amino acids (Fig. 3b). The aforementioned findings demonstrated that CDs exhibit strong selectivity for $O_2^{\bullet-}$ and was not interfered by other active substances. This suggests that the synthesized CDs exhibit a specific response to $O_2^{\bullet-}$. It provides a basis for the application of CDs in cell imaging related experiments.

In order to verify the photostability of CDs, 50 μM $O_2^{\bullet-}$ was added to CDs, and the change of I_{650}/I_{485} fluorescence ratio of CDs with time was measured under the condition of UV lamp irradiation. The experiments have showed that the CDs owned a small change in fluorescence intensity within 60 min before and after the reaction, and were able to emit light for a long period of time, showing good photostability (Fig. 3c).

Detection of $O_2^{\bullet-}$ in human serum

To investigate CDs' potential in real-world uses, the synthesised fluorescent probes were used to determine $O_2^{\bullet-}$ concentration in human serum samples. As shown in the Table 1, $O_2^{\bullet-}$ in human serum samples was detected by CDs with recoveries in the range of 95.2–104% and RSD below 3.9%. These results showed that $O_2^{\bullet-}$ could be detected with CDs in actual serum samples. The above facts indicated that the method has good reliability and stability in the determination of $O_2^{\bullet-}$ levels in serum.

Table 1 Determination of $O_2^{\bullet-}$ concentration in human serum samples (n = 3)

Added (μM)	Detected (μM)	Recovery (%)	RSD (%)
0	1.3	—	2.2
10	10.4	104	3.9
25	23.8	95.2	1.6
50	48.6	97.2	1.2

Live cell imaging of endogenous $O_2^{\bullet-}$

The biocompatibility of nanoprobes is important for their further biological applications, especially in intracellular imaging, thus, a cell viability assay was conducted to evaluate the biocompatibility of the probe, in order to determine whether CDs could be used for $O_2^{\bullet-}$ bioimaging in living cells. CDs at different dilutions were added to normal human hepatocytes LO2. The MTT assay was utilized to conduct cytotoxicity testing, refer to Section S3 in the ESI.† The findings demonstrated that LO2 cell viability stayed above 85% at various dilutions, suggesting that the CDs was extremely biocompatible for detecting endogenous $O_2^{\bullet-}$ in cells. (Fig. S6, ESI†).

$O_2^{\bullet-}$ is an important reactive oxygen species catalyzed by NADPH oxidase 4 (NOX4), which is generated by a mechanism that involves the acquisition of electrons from NADPH and their transfer to molecular oxygen *via* NOX4. The results suggest that $O_2^{\bullet-}$can be used as a specific biomarker to distinguish normal hepatocytes from HIRI hepatocytes. Based on its unique chemical-biological properties, $O_2^{\bullet-}$ provides an important visual assay for real-time dynamic monitoring of changes in ROS levels during HIRI, and shows promising applications in clinical diagnosis and prognostic assessment. In addition, the in-depth study of NOX4 inhibitors is of great scientific significance for the precise regulation of $O_2^{\bullet-}$ generation and its related pathophysiological processes.

Utilizing these outstanding properties of CDs, we investigated their potential for real-time fluorescence imaging of intracellular $O_2^{\bullet-}$ dynamics. To investigate the reversible response behavior of CDs in LO2 cells, 2-methoxyestradiol (2-Me) (3.0 μg mL^{-1}) was first used as a stimulant to increase the concentration of $O_2^{\bullet-}$ in the cells, and then CDs were co-cultured with LO2 cells,[39] and GSH was utilised to restore intracellular redox homeostasis.

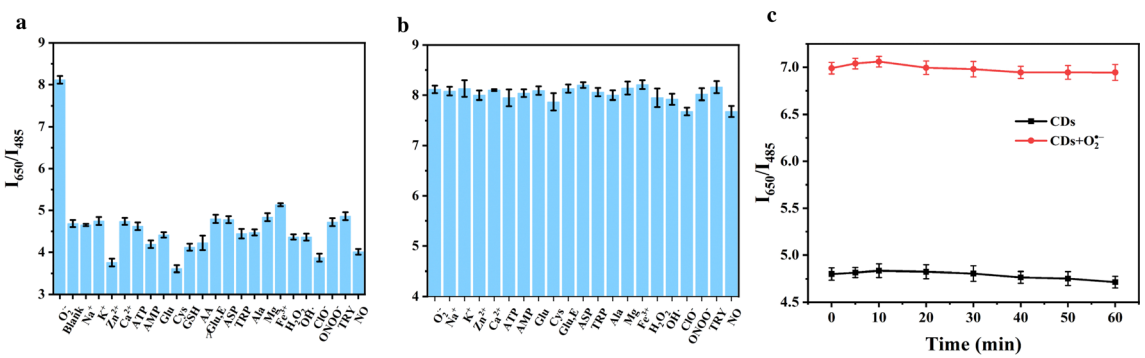

Fig. 3 (a) Fluorescence response spectra of various active species-containing CDs. (b) Fluorescence spectra of different active species added to the CDs/$O_2^{\bullet-}$ system. (c) Changes in the ratio of I_{650}/I_{485} between CDs and CDs/$O_2^{\bullet-}$ systems after 1 h of continuous irradiation under UV lamps.

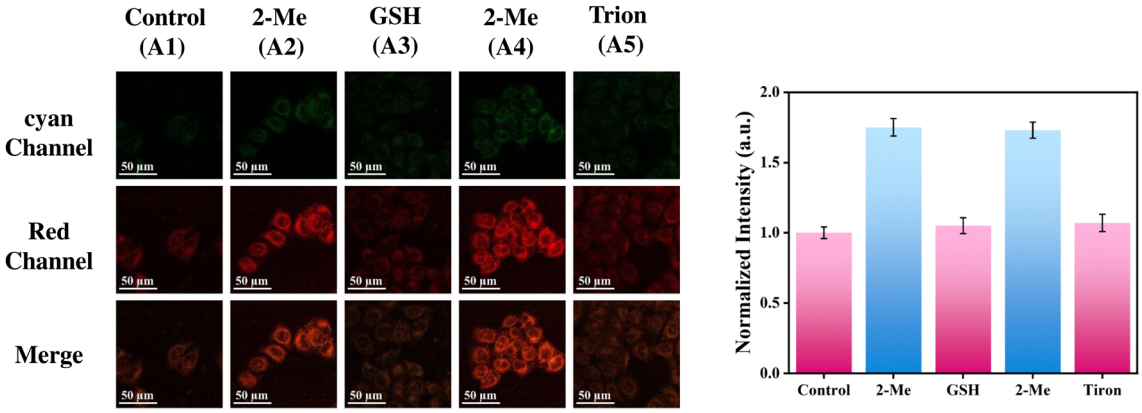

Fig. 4 CDs intracellular reversible imaging (a) control (A1): LO2 cells incubated with CDs for, 2-Me (A2): 3.0 μg mL^{-1} 2-Me was added to the cells on top of A1, GSH (A3): addition of 1.0 mM GSH to A2, 2-Me (A4): 3.0 μg mL^{-1} 2-Me was added to A3 group, Tiron (A5): A4 was supplemented with 10 μM Tiron and incubated for 30 minutes.

It has been observed that after 2-Me stimulation, the intracellular red fluorescence was significantly enhanced, but intracellular cyan fluorescence remained relatively unchanged, this suggests that intracellular $O_2^{\bullet-}$ concentration was elevated. (Fig. 4A2). In contrast, the red fluorescence intensity was significantly reduced upon the addition of GSH. (Fig. 4A3), indicating a decrease in intracellular $O_2^{\bullet-}$ concentration, and two reversible cycles could be achieved (Fig. 4A1–A4). To further demonstrate that the fluorescence enhancement of the probe originated from $O_2^{\bullet-}$, the specificity of the probe was again determined using the specific scavenger Tiron,[40] which cleared $O_2^{\bullet-}$ and resulted in a significant attenuation of red fluorescence (Fig. 4A5). These findings validate, at the cellular level, the ability of CDs to selectively and reversibly detect and observe $O_2^{\bullet-}$, thus enabling real-time dynamic analysis of superoxide fluctuations.

Building upon the exceptional intracellular imaging properties of CDs, we systematically investigated the temporal dynamics of $O_2^{\bullet-}$ generation during HIRI. As a prevalent clinical complication in hepatic surgery, HIRI has been well-documented to correlate strongly with oxidative stress-mediated cellular damage. The dynamics of $O_2^{\bullet-}$ during HIRI were studied using CDs. A HIRI cell model was established to study the changes of $O_2^{\bullet-}$ in HIRI hepatocytes, when compared to the control of the normal group, the HIRI model's hepatocytes' red fluorescence was noticeably higher. (Fig. 5), indicating a substantial rise in intracellular $O_2^{\bullet-}$ levels as a result of HIRI. Our observations was consistent with previous reports that hepatic oxidative stress is associated with hepatocyte injury.

The NOX4 protein is capable of accepting electrons from NADPH and transporting them to O_2 to produce $O_2^{\bullet-}$.[41] Previous experiments have shown the presence of excess $O_2^{\bullet-}$ during HIRI, Therefore, it was investigated whether the excess $O_2^{\bullet-}$ during HIRI originated from NOX4. Upon addition of the NOX4 inhibitor, GKT137831, the red fluorescence was significantly reduced, suggesting that the inhibition of NOX4 led to a reduction in $O_2^{\bullet-}$ levels (Fig. 6). Therefore, it was demonstrated that the excess $O_2^{\bullet-}$ in HIRI cells originated from NOX4.

Conclusions

To address the question of the role of $O_2^{\bullet-}$ concentration changes in the mechanisms related to the development of HIRI

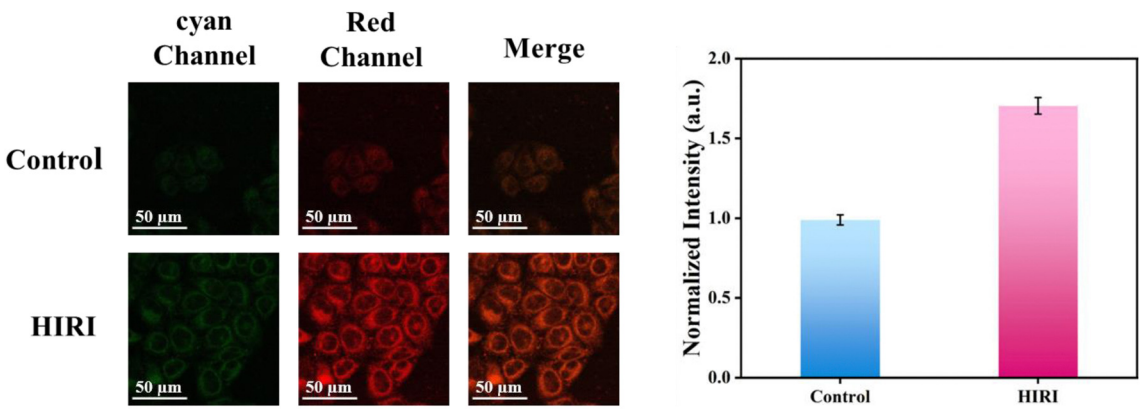

Fig. 5 CDs imaged in HIRI cells: control group: LO2 cells incubated with CDs for 90 min. HIRI group: LO2 cells were added to safener-treated sugar-free DMEM medium and incubated for 15 min, and then normal DMEM medium was added and incubated for 15 min before being incubated with CDs for 90 min for fluorescence imaging.

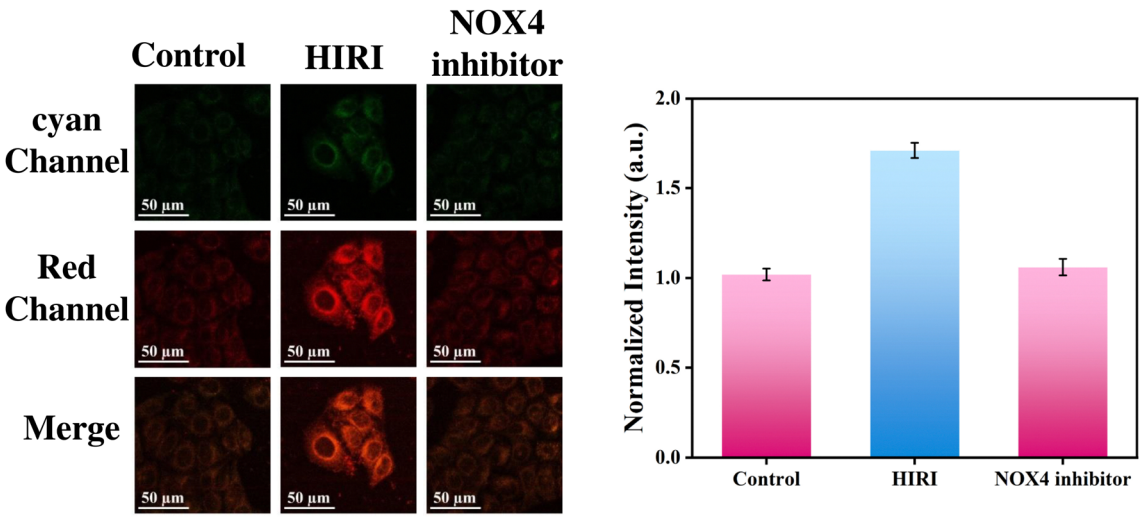

Fig. 6 Control group: LO2 cells incubated with CDs for 90 min, HIRI group: HIRI cells incubated with CDs for 90 min. NOX4 inhibitor group: HIRI cells were first stimulated by adding 2 μg mL^{-1} of NOX4 inhibitor to the cells, and then HIRI cells were incubated with CDs for 90 min before washing and fluorescence imaging of live cells using confocal microscopy.

generation, we designed and synthesised a fluorescent CDs with dual-color fluorescent and reversible imaging to detect $O_2^{\bullet-}$, and found that the $O_2^{\bullet-}$ level was abnormally elevated in HIRI cells compared to normal LO2 cells through fluorescence imaging, and then investigated the role of NOX4 in the process of $O_2^{\bullet-}$ generation. In conclusion, the probe is simple to synthesise and highly sensitive, making it an ideal tool for early clinical diagnosis of HIRI. The design and synthesis of this CDs is expected to provide a new method for the detection of ROS can be used as a powerful analytical tool for the study of diseases associated with intracellular redox homeostasis.

Author contributions

Dan Wang: methodology, conceptualization, writing – original draft. Yanke Zhai: formal analysis, verification. Yun Wang: validation. Xu Fu: supervision, writing review. Yibing Ji: supervision, funding acquisition, writing – review & editing. Ruijun Li: supervision, funding acquisition, writing – review & editing.

Data availability

The data supporting this article have been included as part of the ESI.†

Conflicts of interest

There are no conflicts to declare.

Acknowledgements

This work was financially supported by the National Natural Science Foundation of China [No. 21804141].

Notes and references

1 Y. Zhai, H. Petrowsky, J. C. Hong, R. W. Busuttil and J. W. Kupiec-Weglinski, *Nat. Rev. Gastroenterol. Hepatol.*, 2012, **10**, 79–89.
2 H. K. Eltzschig and T. Eckle, *Nat. Med.*, 2011, **17**, 1391–1401.
3 T. Yoshitomi and Y. Nagasaki, *Adv. Healthcare Mater.*, 2014, **3**, 1149–1161.
4 J. Liu and K. Man, *Cell. Mol. Gastroenterol. Hepatol.*, 2023, **15**, 1463–1474.
5 M. Cannistrà, M. Ruggiero, A. Zullo, G. Gallelli, S. Serafini, M. Maria, A. Naso, R. Grande, R. Serra and B. Nardo, *Int. J. Surg.*, 2016, **33**, S57–S70.
6 S. Zhang, S. Rao, M. Yang, C. Ma, F. Hong and S. Yang, *Int. J. Mol. Sci.*, 2022, **23**, 2357.
7 C. Nastos, K. Kalimeris, N. Papoutsidakis, M.-K. Tasoulis, P. M. Lykoudis, K. Theodoraki, D. Nastou, V. Smyrniotis and N. Arkadopoulos, *Oxid. Med. Cell. Longevity*, 2014, **2014**, 906965.
8 Y. Guan, W. Yao, K. Yi, C. Zheng, S. Lv, Y. Tao, Z. Hei and M. Li, *Small*, 2021, **17**, 2007727.
9 J. Huang, S. Xian, Y. Liu, X. Chen, K. Pu and H. Wang, *Adv. Mater.*, 2022, **34**, 2201357.
10 Y. Geng, Z. Wang, J. Zhou, M. Zhu, J. Liu and T. D. James, *Chem. Soc. Rev.*, 2023, **52**, 3873–3926.
11 B. C. Dickinson and C. J. Chang, *Nat. Chem. Biol.*, 2011, **7**, 504–511.
12 J. George, Y. Lu, M. Tsuchishima and M. Tsutsumi, *Redox Biol.*, 2024, **75**, 103258.
13 Y. Zhao, X. Hu, Y. Liu, S. Dong, Z. Wen, W. He, S. Zhang, Q. Huang and M. Shi, *Mol. Cancer*, 2017, **16**, 79.
14 S.-P. Tang, X.-L. Mao, Y.-H. Chen, L.-L. Yan, L.-P. Ye and S.-W. Li, *Front. Immunol.*, 2022, **13**, 870239.
15 S. Wang, W. X. Ren, J.-T. Hou, M. Won, J. An, X. Chen, J. Shu and J. S. Kim, *Chem. Soc. Rev.*, 2021, **50**, 8887–8902.

16 Q.-J. Duan, Z.-Y. Zhao, Y.-J. Zhang, L. Fu, Y.-Y. Yuan, J.-Z. Du and J. Wang, *Adv. Drug Delivery Rev.*, 2023, **196**, 114793.
17 Z. Ullah, S. Roy, S. Muhammad, C. Yu, H. Huang, D. Chen, H. Long, X. Yang, X. Du and B. Guo, *Biomater. Sci.*, 2024, **12**, 3765.
18 X. Liu and Y.-T. Chang, *Chem. Soc. Rev.*, 2022, **51**, 1573–1591.
19 W. Zhang, J. Liu, P. Li, X. Wang, S. Bi, J. Zhang, W. Zhang, H. Wang and B. Tang, *Biomaterials*, 2019, **225**, 119499.
20 Z. Jie, J. Liu, M. Shu, Y. Ying and H. Yang, *Talanta*, 2022, **236**, 122892.
21 W. Song, B. Dong, Y. Lu, Z. Li, W. Zhang and W. Lin, *Sens. Actuators, B*, 2021, **332**, 129537.
22 Q.-Q. Wang, S.-P. Wu, J.-H. Yang, J. Li, X.-Y. Sun, T.-T. Yang and G.-J. Mao, *Microchem. J.*, 2024, **200**, 110288.
23 W. Zhang, W. Fan, X. Wang, P. Li, W. Zhang, H. Wang and B. Tang, *Anal. Chem.*, 2023, **95**, 8367–8375.
24 C. Xu, W. Zhang, R. Wang, S. Tan, J. M. Holub and B. Tang, *Anal. Chem.*, 2021, **93**, 9111–9118.
25 T. Han, Y. Wang, S. Ma, M. Li, N. Zhu, S. Tao, J. Xu, B. Sun, Y. Jia, Y. Zhang, S. Zhu and B. Yang, *Adv. Sci.*, 2022, **9**, 2203474.
26 Y. Wang, X. Li, S. Zhao, B. Wang, X. Song, J. Xiao and M. Lan, *Coord. Chem. Rev.*, 2022, **470**, 214703.
27 W. Zhang, J. Zhang, P. Li, J. Liu, D. Su and B. Tang, *Chem. Sci.*, 2019, **10**, 879–883.
28 A. T. Krasley, E. Li, J. M. Galeana, C. Bulumulla, A. G. Beyene and G. S. Demirer, *Chem. Rev.*, 2024, **124**, 3085–3185.
29 Y. Jiang, T. Zhao, W. Xu and Z. Peng, *Carbon*, 2024, **219**, 118838.
30 S. Li, L. Li, H. Tu, H. Zhang, D. S. Silvester, C. E. Banks, G. Zou, H. Hou and X. Ji, *Mater. Today*, 2021, **51**, 188–207.
31 H. Liu, X. Zhong, Q. Pan, Y. Zhang, W. Deng, G. Zou, H. Hou and X. Ji, *Coord. Chem. Rev.*, 2024, **498**, 215468.
32 W. Zhang, R. Wang, W. Liu, X. Wang, P. Li, W. Zhang, H. Wang and B. Tang, *Chem. Sci.*, 2018, **9**, 721–727.
33 J. Liu, W. Zhang, C. Zhou, M. Li, X. Wang, W. Zhang, Z. Liu, L. Wu, T. D. James, P. Li and B. Tang, *J. Am. Chem. Soc.*, 2022, **144**, 13586–13599.
34 W. Zhang, P. Li, F. Yang, X. Hu, C. Sun, W. Zhang, D. Chen and B. Tang, *J. Am. Chem. Soc.*, 2013, **135**, 14956–14959.
35 T. Li, D. Wang, J. Hu, X. Fu, Y. Ji and R. Li, *Biosens. Bioelectron.*, 2023, **238**, 115576.
36 X. Sun, C. Brückner and Y. Lei, *Nanoscale*, 2015, **7**, 17278–17282.
37 Y. Xing, Y. Xu, Y. Lin, E. Shuang, H. Leng, J. Wang and X. Chen, *J. Colloid Interface Sci.*, 2023, **640**, 626–636.
38 Z. Liu, X. Zhou, Y. Miao, Y. Hu, N. Kwon, X. Wu and J. Yoon, *Angew. Chem., Int. Ed.*, 2017, **56**, 5812–5816.
39 Y. Zhou, E. O. Hileman, W. Plunkett, M. J. Keating and P. Huang, *Blood*, 2003, **101**, 4098–4104.
40 T. M. H. Dourado, V. O. Assis, W. M. C. Awata, M. M. B. de Mello, E. C. Cárnio, M. M. Castro and C. R. Tirapelli, *Eur. J. Pharmacol.*, 2023, **949**, 175723.
41 J. Liu, W. Zhang, X. Wang, Q. Ding, C. Wu, W. Zhang, L. Wu, T. D. James, P. Li and B. Tang, *J. Am. Chem. Soc.*, 2023, **145**, 19662–19675.

